2021 International Conference on Unmanned Aircraft Systems (ICUAS)
Athens, Greece. June 15-18, 2021

The MiniHawk-VTOL: Design, Modeling, and Experiments of a Rapidly-prototyped Tiltrotor UAV

Stephen J. Carlson, Christos Papachristos

***Abstract*— This work addresses the rapidly-prototyped design of a small Tricopter/Fixed-Wing Vertical Take-Off and Landing UAS with solar-recharge-capability, capable of repeatedly landing, recharging, and taking off, without need for physical intervention or externally placed maintenance devices or platforms. The design uses Fused Deposition Modeling 3D printing to rapidly prototype and fabricate the majority of the aircraft structures and parts. Provisions are made for carrying high-level single board computing solutions, or other similar payloads. Details are provided for mechanisms, aerodynamic geometry, solar cell integration and manufacturability. The design is analyzed to estimate inertial moments, aerodynamic performance, and static and dynamic stability. Simulation models for the Gazebo and RealFlight environments are provided, targeting Software-In-The-Loop architectures that run the ArduPilot and PX4 flight stacks. A flight testing methodology is developed, and results are presented with multiple prototype vehicles constructed. We finally contribute all production definitions, files, and models as open-access resources, with the goal of supporting and promoting migratory/swarming behavior and autonomy research.**

2021 International Conference on Unmanned Aircraft Systems (ICUAS) | 978-1-6654-1535-4/21/$31.00 ©2021 IEEE | DOI: 10.1109/ICUAS51884.2021.9476731

I. INTRODUCTION

A significant body of work related to Unmanned Aerial Systems (UAS) research over recent years has been dedicated to address the needs of multi-envelope aircraft design and control [1–8] in order to facilitate versatile aerial robot platforms which can accomplish combined operational profiles. As a contribution to this field, the MiniHawk-VTOL is presented within this work: A small (sub-meter wingspan, sub-kg mass) Vertical Take-Off and Landing (VTOL) platform, integrating a pair of forward-tilting rotors and a third fixed rotor on the tail, allowing the aircraft to function under both the fixed-wing as well as the stable hovering flight profile.

The primary goal of this proposed design is however to inaugurate the field of migratory UAS research. We define a migratory UAS as any flying robot that has in situ energy harvesting capabilities (such as utilizing integrated solar cells), sufficient ground and aerial locomotive ability for takeoff and landing without human intervention, and adequate sensor capabilities and processing to autonomously navigate unstructured environments. The MiniHawk-VTOL is designed to integrate solar cells embedded in the top wing surface, and combined with its VTOL capability, and sufficient internal volume and payload ability for a perception system, satisfies the basic requirements to develop migratory behavior.

This material is based upon work supported by the NSF Award: AWD-01-00002751: RI: Small: Learning Resilient Autonomous Flight. The presented content and ideas are solely those of the authors.

Special thanks to Adrian Nagy Hinst for his implementation of the MiniHawk-VTOL in RealFlight 9.5, and the tuned .param file.

The authors are with the University of Nevada, Reno, 1664 N. Virginia, 89557, Reno, NV, USA stephen_carlson@nevada.unr.edu

Fig. 1. Solar-Wing variant of the MiniHawk-VTOL. The wing top surface is excavated for the conformal integration of the Maxeon™ solar cell series, including wiring conduit tunnels (hidden).

An important distinction to note in the definition of migratory behavior is that it is not synonymous with continuous flight operation, as discussed in [9]. A migratory vehicle only needs energy sufficiency, not energy superiority as featured by most High-Altitude Long-Endurance vehicles such as the Sky Sailor referenced above, or the Airbus/Qinetiq Zephyr to cite another example. The work by Sherbrooke University with the SUWAVE [10, 11], is a perfect example of a migratory UAS, with its mission cycle alternating between charging on the surface of one lake, taking off vertically, and flying to the next lake in its route, and landing to recharge and repeat the sequence. A terrestrial version of this mission cycle is proposed by [12], and this is precisely what the MiniHawk-VTOL is designed to accomplish.

As acknowledged in [13], when attempting to produce a viable open-access VTOL aircraft definition, the manufacturing process is just as important as the design. The MiniHawk-VTOL avoids the risks and costs associated with milling molds and the time required to do composites material layup and fabrication. This is accomplished by having the *entire* aircraft 3D printed, which is a common and well understood process which only requires a printer and feedstock. Changes to the design do not result in a cascade of re-crafting of molds and related tools, as the structural definition is directly fabricated with no intermediate production steps.

A finished example of the MiniHawk-VTOL is shown in Figure 1. The design (with and without provision for top-surface solar cells) is offered for typical VTOL experimen-

tation. The production files, build instructions and all other artwork are hosted on a GitHub repository at [14].

The rest of this paper is structured as follows. Section II presents the vehicle design, including mechanism geometry and manufacturability considerations. Section III provides performance analysis and predictions. Section IV presents supported simulation ecosystems of our contributed open-source models, and Section V reviews the supported flight-stack avionics and presents experimental results with the fully developed vehicle.

II. AIRCRAFT DESIGN

This work presents significant extension over prior work on hybrid aerial vehicle design [15]. Relevant examples of the state of the art in tricopter tilt-rotor vehicle design can be found in [13, 16], with modeling approach demonstrated in [17, 18].

A. Requirements

The following requirements are observed for the design of the MiniHawk-VTOL:

1) The primary functional requirement is that this must be a Tricopter Tiltrotor Fixed-Wing VTOL.
2) The secondary functional requirement is that the Maxeon™ Solar Cell Series be implemented on the wing surface, enabling migratory behavior experimentation.
3) A payload performance requirement: After essential avionics and propulsion are accommodated, an additional payload mass of 140g, with a bounding box of 120mm by 60mm by 30mm, must be supported.
4) A process requirement is that this aircraft must be Fused Deposition Modeling (FDM) 3D-Printed, utilizing a 0.4mm nozzle with 0.2mm layer height.

The requirement for a Tricopter Tiltrotor topology was driven by past experience, mainly to try to minimize aerodynamic drag in forward-flight, and to reduce costs. In forward-flight, a Tricopter Tiltrotor only has a single stopped rotor, and can have the forward-tilting pair of rotors optimized for forward-flight while retaining modest hover lift capability.

The payload definition was chosen so that the most common companion computers, such as the Raspberry Pi, the Nvidia TX2, and their peers can be flown onboard the aircraft. The volume can also be allocated for a larger battery. Figure 2 shows the notional payload cross-section.

B. Design Decisions and Metrics

1) Structure and Component Mass Allocations: The MiniHawk-VTOL accommodates most flight controllers that use a 30.5mm grid hole mounting pattern. The Matek WING Series and the mRo PixRacer Pro both demonstrate acceptable fit. 60g is assumed for the flight control avionics, including R/C receiver. The MiniHawk-VTOL uses a 3-cell 1300mAh battery, typically 125g. Four Hitec HS-5065MG+ servos are used, at roughly 12g each (substituting with HS-65HB is also acceptable). The forward pair of motors are DYS BE1806-2300KV, each 20g, and the associated ESCs are Spedix ES20 Lite, at 12g each. The rear motor may

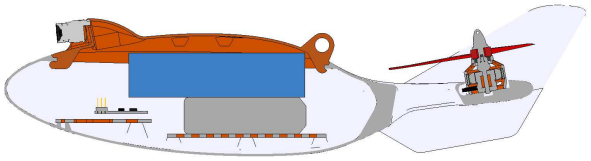

Fig. 2. Section View of the Fuselage. The payload volume is shown in blue, resting on top of the battery, shown in grey.

be any standard drone racing motor, with DYS BE2206-2000KV selected as nominal, with a mass of 35g, and utilizing the same Spedix ESC. Including propellers and linkage mechanisms, the no-payload systems total is rounded up to 360g. The additional payload mass of 140g finalizes the notional systems mass estimate to 500g.

The aircraft total mass was unknown at the beginning of the design process, and it was expected that it would fluctuate between initial estimates and final product. To start, it was estimated that the airframe structures would be 50% of the systems mass total, giving a structures goal of 250g, and 750g as the estimated final vehicle mass. These estimates were low when compared to the final values of the constructed vehicle (see Section II-D.2), but they provided a starting point from which the rotor sizing and aircraft wing geometry could be drawn. Also note that solar cells are lumped into the structures estimate.

2) Rotor Sizing and Thrust Allocations: Rotor thrust allocations during hover were drawn to be roughly 28% thrust for each forward rotor, and 44% thrust contributed from the rear rotor. Each rotor's motor drives a 5-inch (127mm) 3-blade propeller, with the option of using a 6-inch (152mm) for the rear propeller. The forward rotor propeller pitch is chosen for a pitch speed of 20 to 25 m/s, while the rear rotor is optimized for hover and has a lower pitch. The rotor positions form a bounding circle with a circumference of 315mm, with its center resting near the intended Center of Mass.

3) Aerodynamic Geometry: With rotor positions and diameters known, the aircraft planform (wing shape) was decided next. The main two constraints on wing design are avoiding the discs of the rotors, and accommodating the solar cell requirement. Also, the Center of Lift for the wing should coincide with the Center of Lift from the rotors. A "flying wing" with moderate sweep is most conducive to fitting the area of the wing within the discs of the rotors, but it was decided to use the "plank" planform, with zero-degrees wing-sweep angle for the quarter-chord line. This decision allows the nacelles supporting the front rotors to be as short as possible. The initial Center of Mass calculations also supported the plank planform as being more favorable to correct balance and Center of Lift agreement with the rotors.

For the solar wing requirement, the Maxeon™ Series was specified due to its flexibility, enabling conformal embedding

on the top surface of the wing. This ability alleviates having to make the airfoil top surface flat, or to have a transparent window scheme for a submerged array. Each cell is 125mm in width and height [19], and this provides a quanta (interval) for the wing span and chord: The wing chord must accommodate at least one row (125mm high), and span steps for each whole cell. A total count of four cells was arrived at, as a compromise between improving both aspect ratio and wing area, verses increasing total aircraft mass. The aircraft wing span for this condition is 800mm tip-to-tip. We note here that four cells should produce 14 Watts in ideal conditions, which is acceptable for energy sufficiency.

While flexible solar cells are useful for this design, the technology still carries geometry constraints: For the solar cells to conform without wrinkles, the placement surface must be geometrically developable (defined as a surface with Gaussian Curvature equal to zero for all points). The final solar cell placement and Gaussian Curvature is shown in Figure 3; while Gaussian Curvature is not zero for the entire region, it is sufficiently small to lend confidence that the solar cells will wrap correctly. The Non-Zero Gaussian Curvature is a result of the root-to-tip washout and boundary conditions applied to the loft/blend.

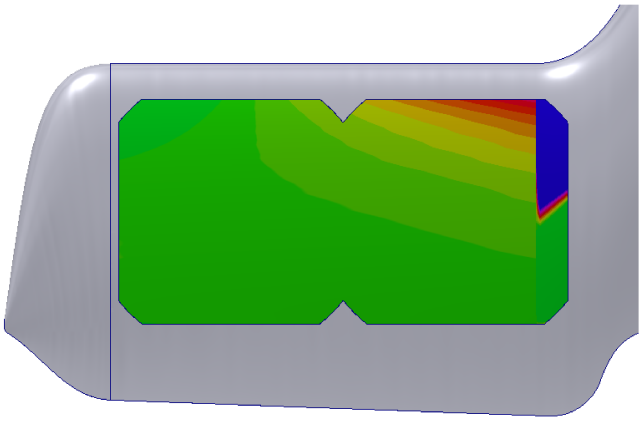

Fig. 3. Gaussian Curvature of the Solar Cell Excavation Surfaces. Green regions have Gaussian Curvature = 0. Negative values of Gaussian Curvature progress to Red and Blue, forming a very slight hyperbolic/saddle shape.

The MH45 airfoil [20] was selected for the root and tip profiles, given its low C_m across most positive values of α, and excellent efficiency at Reynolds numbers at and above Re=100k. At the root chord, the profile is pitched up 1.33deg, and the tip profile is pitched down 0.52deg, with washout angle total of 1.85deg. The leading edge of the wing is straight and perpendicular to the longitudinal axis. After finalizing the wing shape, the projected wing area is 15.6dm^2, with Mean-Aerodynamic-Chord of 195mm, and aspect ratio of 4.1. Provided that the final vehicle mass is 750g, the wing loading is around 50$grams/dm^2$.

The rear rotor is mounted with its thrust axis canted forward 10 degrees from vertical, to allow for a smoother entry into forward-flight during VTOL transition. This also relaxes the total tilt range angle needed for the front tilting mechanism (83 degrees from Hover Mean to Forward Flight). The forward motors are canted down 3.00deg, to correspond with the estimated level cruising-flight attitude.

Table I lists the design parameters for the project. Note that the coordinate convention used is Construction-Frame, which is described further in Section III-A.

TABLE I
MINIHAWK-VTOL DESIGN PARAMETERS

Category	Parameter	Value	Units
Wing Root	X Offset (tip)	0	mm
	Y Offset	100	mm
	Chord	200	mm
	Twist Angle	1.33	deg
	Airfoil	MH45	
Wing Tip	X Offset (tip)	0	mm
	Y Offset	340	mm
	Chord	190	mm
	Twist Angle	-0.52	deg
	Airfoil	MH45	
Planform	Wing Span	800	mm
	Wing Area (projected)	15.6	dm^2
	MAC	195	mm
	Aspect Ratio	4.1	
	C/4 Sweep	-0.5	deg
	Dihedral	0	deg
Forward Rotors	X Offset	-60	mm
	Y Offset (+/-)	120	mm
	Diameter	127	mm
	Thrust Angle (fwd-flt)	-3.0	deg
	Tilt Range (typical)	87	deg
Rear Rotor	X Offset	200	mm
	Diameter	153	mm
	Thrust Angle	80.0	deg
Bounding Circle	Diameter	315	mm
	X Offset (center)	42	mm
Other Measurements	Length	396	mm
	Body Volume (approx)	1000	cm^3
	OML Volume (approx)	2900	cm^3

4) Mechanisms: Two nacelles are used for mounting the forward pair of tilting rotors, and conducting thrust forces to the airframe. The linkage for each is a Non-Grashof Triple-Rocker, proportioned such that a Top-Dead-Center condition occurs at the servo when the respective motor is in the forward-flight position. This condition is shown in Figure 4. This is intended as a kind of locking mechanism to alleviate servo torque stresses while in forward-flight for long intervals.

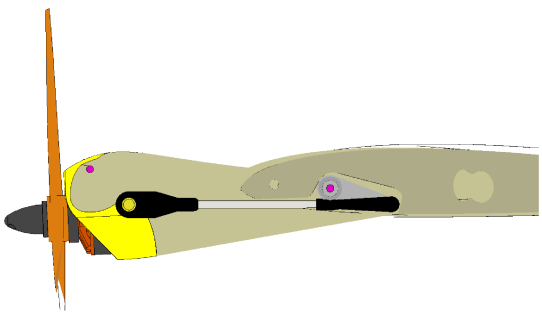

Fig. 4. Nacelle Linkage in TDC Condition. Fixed pivots are colored in magenta.

The rotor tilt linkage has a non-linear relationship between the driving servo arm angle and the motor tilt angle. The linkage lengths are selected such that when the vehicle is in the hover condition, the motor tilt angle transfer function is roughly linear, with respect to servo input. The Input-Output relationship curve is shown in Figure 5. The equation for tilt angle is $\theta_{output} = (-0.000126)\cdot\theta_{servo}^3 + (0.016071)\cdot\theta_{servo}^2 + (0.038604)\cdot\theta_{servo} - 0.991229$, where input and output are in degrees. The total tilt travel is typically 87 degrees (servo traveling 95 degrees), allowing for yaw control by differentially tilting each rotor up to +/- 4 degrees to contribute a torquing moment on the airframe. This differential tilt margin is non-symmetric; a stable trimmed hover requires some bias to counter torque from the rear rotor, which means yaw commands for one direction may saturate sooner than the other. Typically, there is sufficient yaw authority for both directions that this artifact is not encountered.

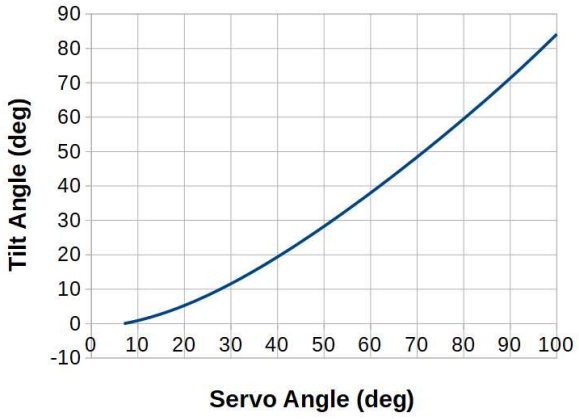

Fig. 5. Motor Tilt Linkage Plot. Tilt angle of zero corresponds to forward-flight (front motor flush inside nacelle, canted down 3.0 deg). A tilt angle of 83 degrees is colinear with the rear rotor thrust axis.

Using the linkage to control the motor tilt angle requires an important consideration for tilt servo torque strength. The torque on the servo, T_{servo}, is roughly related to the thrust, F_{rotor}, by the equation $T_{servo} = F_{rotor} * (L_{1a}/L_{1b}) * L_2$. The values of L_{1a}, L_{1b}, and L_2 are the offsets between motor thrust axis and tilt axis, tilt axis and linkage ball-joint, and the servo arm, respectively. These measurements are 14.5mm, 16mm, and 19mm respectively. For F_{rotor} less than 5N, this is less than 0.09 Nm, which is within the torque rating of the HS-5065MG+ (0.18 Nm), with considerable margin.

C. Feature Implementation up to Outer Mold Line (OML)

The body cavity is sized to contain the battery, avionics, and the primary payload. The avionics are directly accessible, and the empennage/tail has a cutout to alleviate wasted thrust effort, and to strengthen the structure.

The wings have two variations: The Solar-embedded variant for the Maxeon™ Series as described above, and a Non-Solar wing for typical flight testing. Wire conduits are contained completely within each wing, such that the top and bottom surfaces are uninterrupted. Each wingtip contains a pocket for a single SMD 5050 LED. A wire conduit runs to the pocket, allowing for a 3- or 4-wire addressable device to be driven.

The vertical stabilizer projected area was undersized initially, and the design subsequently had strakes added during the course of flight testing. Each fin terminates on the top surface without intersecting the solar cell area partitions.

The hatch, or lid, is designed to seal to the lip formed in the upper body cavity. A mild hook catches the inside of the rear lip with mechanical friction, allowing for installation and removal by hand. Several hatch variations exist for different use conditions, such as video telemetry transmission or GPS+Pitot-Probe.

D. Post-OML Tweaks and Manufacturability

The aircraft must have various geometry modifications for it to work correctly. These are consequences of selecting FDM as the fabrication method. These issues are related to the process itself, the material used, or the constraints of the printing device.

1) FDM Process Issues: FDM uses an extruded filament of thermoplastic material to additively form a part. As a consequence of the additive process, the thermoplastic must be supported and avoid overhangs or severe slopes. A normal FDM workflow will typically generate support material for these overhangs, but in many instances, this is very inefficient or compromises the part being fabricated. Also of critical observation is that parts printed have a grain, or layer orientation, which introduces an anisotropy to the part.

Acknowledging the overhang problem, the MiniHawk-VTOL is sectioned into various pieces, such that each piece can be printed from a level print bed, as is intrinsic to most 3D printers. The servo pockets in the wing are vaulted with a draft angle that prevents overhang droop, and various other overhangs are drafted to alleviate the issue. The empennage/tail pieces have explicit overhang support definitions, which are sacrificial and are removed after fabrication.

The inherited anisotropy property is addressed for most sections by aligning the strength axis to the layer direction; such is the case with the nacelle and empennage/tail pieces. However, for other parts such as the wings, the layer direction must be aligned such that the wing surface is a smooth closed loop for each layer, forfeiting the improved strength that could otherwise be enjoyed.

For the wing elevons, small gaps were introduced at the boundaries between the control surface and the structure of the wing trailing edge. These are 0.2mm in width, corresponding to a single layer omission assuming the wing is printed from root to tip. This will generally aid in separating or breaking the elevons free, by presenting a mild gap between layers.

The moving parts on the MiniHawk-VTOL have had tolerance offsets applied to moving/sliding surfaces, such as the nacelle motor pocket. These tolerances were found by trial and error after many iterations.

2) Print Material Issues: The MiniHawk-VTOL uses a living hinge scheme for the elevons. This is re-enforced with

off-the-shelf nylon hinges due to the fact that PLA, the most common print material for FDM printers, tends to fracture and break. PLA with acrylic additives tends to perform better but will ultimately also break. Printing the wing with other materials may alleviate this.

While FDM allows this design to be reproduced by any party, this advantage has a primary drawback in the final weight of the vehicle. As shown in Section II-B.1, the initial target for the airframe structural mass was 250g, but in the current version, the vehicle structures total to around 400g when printed using $1.25g/cm^3$ material.

3) Print Volume Considerations: As visited in Section II-D.1, partitioning of the project into pieces is necessary for material support. A secondary partitioning is necessary in cases where the printer build dimensions are too small to fit a section. The MiniHawk-VTOL wings present the largest part, at 330m height and 211mm chord each.

III. DESIGN ANALYSIS

In this section we provide a thorough aerodynamic analysis over the previously presented UAS design.

A. XFLR5 Model and Analysis

XFLR5 [21] is an analysis tool for airfoils and aircraft structures operating at low Reynolds Numbers. It is useful in estimating the performance parameters, static and dynamic stability, and inertial parameters of an aircraft design. The XFLR5 model of the MiniHawk-VTOL is shown in Figure 6. Note that the coordinate system used in XFLR5 is Construction-Frame convention, with X-coordinate increasing from nose to tail and Z-coordinate increasing upward. Also note that the Construction Frame origin is centered at the leading edge of the wings.

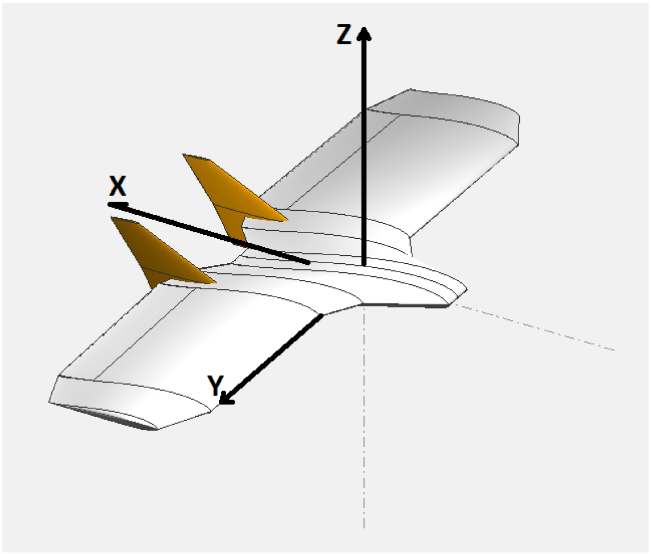

Fig. 6. XFLR5 Model

1) Static Stability and Trim Condition: Before the performance of the aircraft can be established, the XFLR5 model needs to be trimmed for level flight. This has two components: Making the model stable in pitch, and adjusting control surfaces to result in a reasonable trim equilibrium speed. Both of these activities are unaffected by the inertial properties of the aircraft, but the results will affect the mass distribution and modeled aircraft geometry.

The Neutral Point was determined in XFLR5 by forcing the Center of Mass as a driven parameter, and sweeping this value while observing the plot of the Pitching Moment as a function of α. The Neutral Point is found at X=35mm, and an initial X_{CoG} is fixed to X=32mm. The equilibrium speed must be very high at this configuration, corresponding to the X-intercept on the Pitching Moment plot being very close to α=0. The X-intercept is raised by incrementing the angle on the modeled elevons. The model was brought to an equilibrium of α=2.0deg by setting the elevons to -1.0deg (up). This is shown in Figure 7.

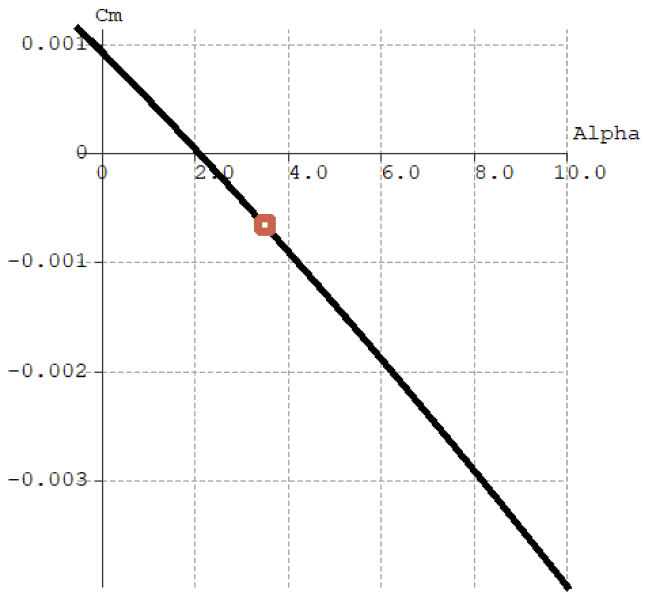

Fig. 7. Pitching Moment Plot. Center of Mass located at 32mm behind wing leading edge, elevons set to -1.0deg (up). Marker indicates the 3.5 degree positive alpha op-point.

2) Inertial Properties: After establishing the final trim of the model, the inertial parameters can be estimated for the MiniHawk-VTOL. The position and mass for each component are taken from the CAD model assembly. Note that the entry "Nose Lead" was not an original member of the CAD assembly, and is a result of the trim study, where X_{CoG} is brought to a value of 32mm by incrementing the Nose Lead value.

The values from Table II are used for finding the principle moments of inertia for the vehicle, centered at the Center of Mass. XFLR5 provides an inertial model for the wing, albeit modeled as a homogeneous solid. Although the fabricated

TABLE II

POINT-MASS MODEL

Component	mass(g)	x(mm)	y(mm)	z(mm)
Wing	350	61	0	2
Right Tilt Servo	11	32	155	-5
Left Tilt Servo	11	32	-155	-5
Right Elevon Servo	11	95	155	-5
Left Elevon Servo	11	95	-155	-5
Rear Motor	35	200	0	10
Right Motor	20	-45	120	-10
Left Motor	20	-45	-120	-10
Battery	140	40	0	0
Avionics and Cam	70	-60	0	0
ESCs & Wires	50	-10	0	0
Nose Lead	51	-110	0	3
Total	780			
Center of Mass		31.6	0	0.7

wing is a thin-shell with infill, this approximation is deemed acceptable. Table III below shows the estimated Principle Inertial Moments for the vehicle as defined in the above mass model.

TABLE III

COG-FRAME INERTIAL MOMENTS

Component	Ixx($kg \cdot m^2$)	Iyy($kg \cdot m^2$)	Izz($kg \cdot m^2$)
Wing only	0.015	0.001	0.016
Entire Vehicle	0.017	0.004	0.021

3) Flight Performance and Dynamic Stability: With aircraft inertial properties captured, and a rough trim of the elevons= -1deg, the flight performance can be estimated. The Lift/Drag curve is shown in Figure 8; this shows the effective glide ratio of the aircraft for a given pitch angle. It is noted that the peak of 15.7 is somewhat suspect; a value closer to 10 or less would be expected for this design. This is likely because the XFLR5 model does not include much of the parasitic drag that the actual aircraft experiences, in the form of skin and interference drag.

The power curve is shown in Figure 9. From this curve, two efficiency speeds can be drawn: The airspeed for Minimum-Power-Required for longest flight-time, $V_{min_{P_R}}$, and the airspeed for Power-Required at Maximum L/D, $V_{(L/D)_{max}}$. The former is useful for loiter operations, and the latter is useful for maximum range. $V_{min_{P_R}}$ occurs at the trough of the curve, while $V_{(L/D)_{max}}$ occurs at the intersection of a line drawn from the origin and tangent to the curve. Again, without skin and interference drag in the XFLR5 model, these values are rough estimates.

From [21], the longitudinal dynamics of the vehicle can be estimated in XFLR5. The Short-Period and Phugoid time constants are solved from the inertial model and aerodynamic polars, and the ratio between the numerical frequencies of the Short-Period and Phugoid modes corresponds to the dynamic stability of the aircraft. The dampening factor ζ is also important for determining how oscillations will dissipate. Here, with $F2 = 1.047Hz$ and $F_{ph} = 0.074Hz$, the ratio is approximately 14, which is stable. All these values, and

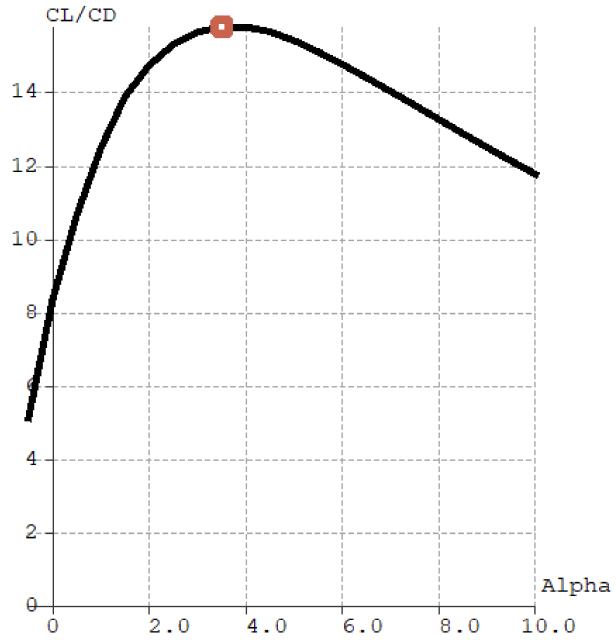

Fig. 8. CL/CD. Marker indicates the 3.5 degree positive alpha op-point.

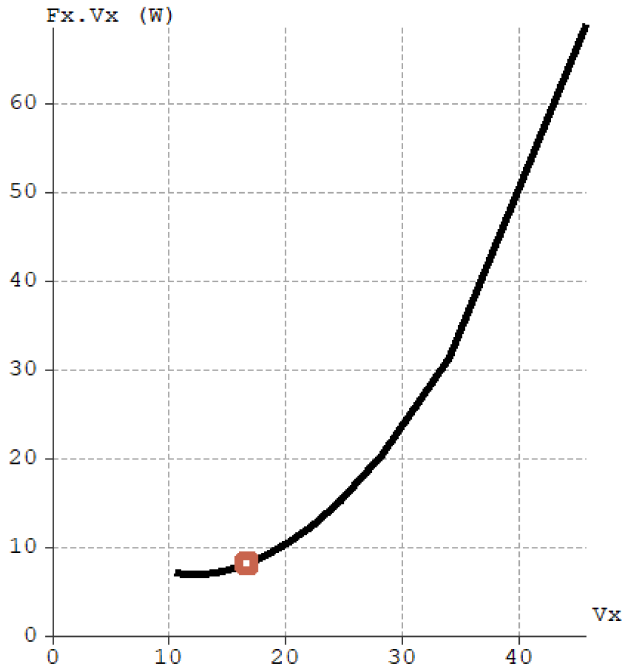

Fig. 9. Power Required. Marker indicates the 3.5 degree positive alpha op-point for best L/D.

the parameters yielded from the XFLR5 study are given in Table IV.

B. Computational Fluid Dynamics Analysis Considerations

While XFLR5 was used as a lightweight analysis tool for the MiniHawk-VTOL, a set of poses of the aircraft

TABLE IV
MINIHAWK-VTOL PERFORMANCE ESTIMATES

Category	Parameter	Value	Units	Notes
Speeds	V_{stall}	11	m/s	α=10 deg
	$V_{min_{P_R}}$	12	m/s	α=7.5 deg
	$V_{(L/D)_{max}}$	17	m/s	α=3.5 deg
Balance	X_{CoG} (nominal)	32	mm	from LE
	X_{CoG} (limit)	35	mm	from LE
Long. Dynam.	F1	1.643	Hz	Short Period
	F2	1.047	Hz	Short Period
	ζ	0.770		Short Period
	F_{ph}	0.074	Hz	Phugoid
	ζ	0.036		Phugoid

were generated for potential Computational Fluid Dynamics (CFD) analysis. The aircraft CAD model geometry was reduced to a fundamental aerodynamic OML (and splitting the vehicle to the left side only), and the elevon angle was incremented across a range of values. STL files were exported for each condition, such that a set of polars can be built up from meshing and simulating the set in a CFD environment.

IV. SIMULATION MODELS

The above analysis allows for the MiniHawk-VTOL to be implemented in simulation models for robotics and flight simulation. Accompanying the inertial and performance metrics, a set of 3D definitions was created specifically for simulation. The CAD assembly geometry was reduced and exported to several sets of STL files, with each set corresponding to a Level-of-Detail between high- and low-fidelity. This is useful for most game engines and simulation environments where graphics performance is preferred over geometric accuracy.

A. Gazebo Model and PX4 SITL

Figure 10 shows our MiniHawk-VTOL simulation model in the Gazebo robotics environment. The model uses the inertial estimates from the XFLR5 analysis for kinematics. The aerodynamics model is implemented using the PX4-SITL_gazebo liftdrag_plugin, which only allows for very simplistic use of the XFLR5 analysis, but does at least model rotors as actuated discs and other improvements over the original Gazebo liftdrag plugin.

B. RealFlight 9.5 and ArduPilot SITL

The RealFlight model of the MiniHawk-VTOL observes the XFLR5 inertial estimates and uses the reduced-geometry STL representations. RealFlight's aerodynamics engine also incorporates the MiniHawk-VTOL airfoil polars and wing geometry. Running a SITL instance of the ArduPilot flight-stack against RealFlight enabled the discovery of a set of parameters and PID coefficients that result in a controllable vehicle. An ArduPilot parameter file of these values is included in the project repository. Figure 11 shows a screenshot the model in action.

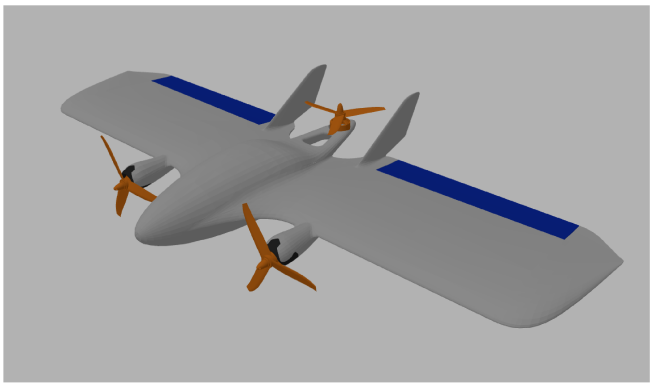

Fig. 10. MiniHawk-VTOL Gazebo Model.

Fig. 11. RealFlight 9.5 Vehicle Model. ArduPlane SITL is used to drive the inputs to the RealFlight simulated vehicle, with the physics simulation incorporating the derived dynamics of the vehicle. Screenshot taken from [22].

V. FLIGHT TESTING AND RESULTS

Two prototypes were constructed. A Creality CR-10 3D Printer was used to print all the airframe components, as shown in Figure 12. Figure 13 shows the fleet. The solar-winged variant was the first built, intended only as a non-flying system integration testbed. The second one built was the flight-test vehicle, which has enjoyed the sum total of all flight time and testing.

Control of this class of vehicles has been broadly addressed in relevant research [17, 23, 24], while additionally being thoroughly documented by the open-source aerial robotics community [25, 26]. The following subsections will detail the process in getting the vehicle to fly, as general flight test process steps, and specific setup for each of the flight stacks used.

A. Flight Testing Steps

Regardless of which flight stack is used (ArduPlane/PX4/Betaflight), the same general sequence is followed for tuning and calibrating the vehicle.

1) Constrained Roll- and Pitch-Axis Testing: The first activity is mounting the vehicle on a suspension of some type, away from any surface which could contribute ground

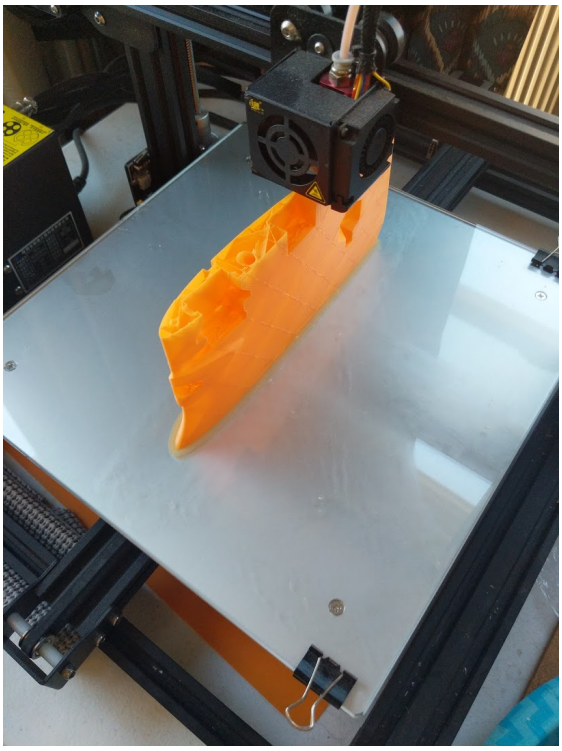

Fig. 12. A photo of the Creality CR-10 printing the left wing of the solar-wing prototype.

Fig. 13. Flight-Test Vehicle (front) and Solar Prototype (rear). Note the enlarged vertical stabilizer surfaces and strakes added on the Flight-Test vehicle to improve directional stability. The Flight-Test vehicle also features a folding rear propeller for improved forward flight drag.

effect (1 meter is sufficient). The roll or pitch axis are mechanically constrained, with the centerline as close to the vehicle Center of Mass as possible. Each test using this suspension should be performed at the hover throttle setpoint, as evidenced by the load on the suspension dissipating. Initially, all PIDs should be zero or minimal; for each axis (roll and pitch), PIDs can be tuned by hand, or through the Ziegler–Nichols Method [27]. The yaw PIDs are left zeroed or minimal, as these are best tuned in a free-flying condition.

2) Free Hover Testing: After tuning on the suspension, the vehicle is test-flown from a level surface. The yaw PIDs are tuned until the aircraft can depart the surface and maintain directional stability, again by hand or using the Ziegler-Nichols Method. The aircraft can then be flown above ground effect and PIDs more finely tuned until hover is stable. The aircraft should mildly weathervane into the relative wind.

3) Constrained Pitch Axis Transition Tuning: Flight stacks such as ArduPilot require an airspeed measurement/estimate for the transition algorithm to work. As such, it is difficult or impossible to discover the controller behavior by constraining the aircraft in the pitch axis and commanding the VTOL tilt sequence to forward-flight. Flight stacks that do not integrate airspeed in the VTOL transition may benefit from this activity otherwise. This is specifically useful for developing a PID gain schedule for each point in the VTOL condition angle between hover and forward-flight.

4) Forward-Flight Transitions and Forward-Flight Tuning: If the Center of Mass is correctly positioned, the vehicle should be dynamically stable in the pitch axis, as shown in Section III. Nonetheless, pitch stability augmentation is very useful if the vehicle is flown by hand, as it is very sensitive to inputs and disturbances in that axis. Transitions to forward-flight should be smooth for both directions.

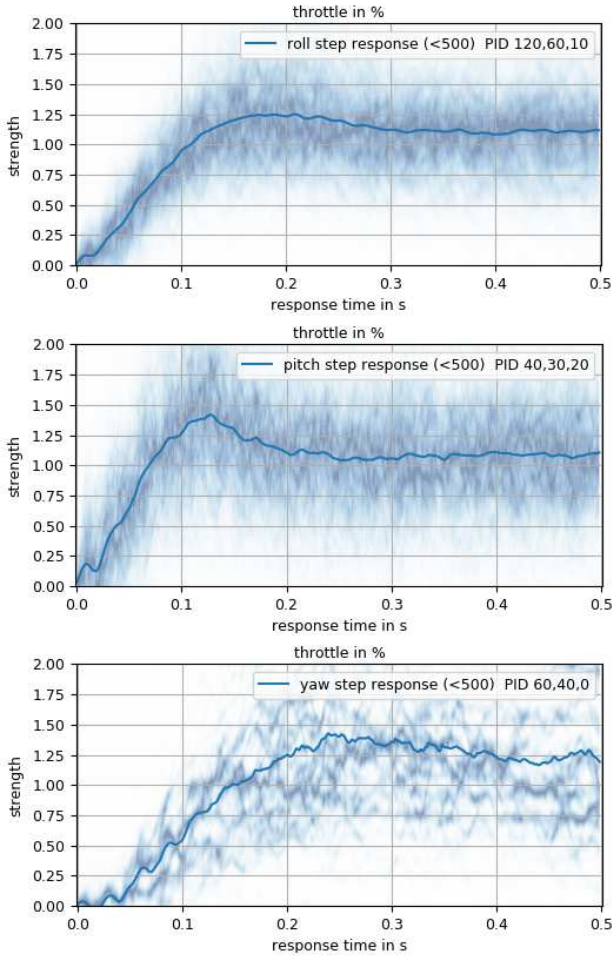

Fig. 14. Step Response for Roll, Pitch and Yaw in Betaflight.

B. Betaflight Results

Following the method prescribed above, the MiniHawk-VTOL was originally flight tested using the Betaflight flight stack. This used the Matek F722-WING flight controller, running a modified version of Betaflight with VTOL mixers and gain scheduling added. Figure 14 shows the step response from a flight test where the vehicle was fed aggressive inputs for roll, pitch and yaw for system characterization.

The VTOL transition in Betaflight was developed far enough that the vehicle could enter and exit forward-flight abruptly; more work remains to polish the mixing and gain scheduling.

C. ArduPlane Results

The ArduPilot/ArduPlane flight stack was implemented on the MiniHawk-VTOL using the mRo PixRacer Pro. The Tricopter/Fixed-Wing hybrid that the MiniHawk-VTOL may be classified as is supported "out-of-the-box" by the firmware [26], with all behaviors configured by user-configurable parameters. The RealFlight parameters found in the simulation environment were used as initial configuration.

Fig. 15. Forward-flight low-pass

Figure 15 shows the vehicle in forward-flight running the ArduPlane flight stack. Figures 16 and 17 show the attitude during a VTOL transition to forward-flight and back to hover over a period of 5 seconds.

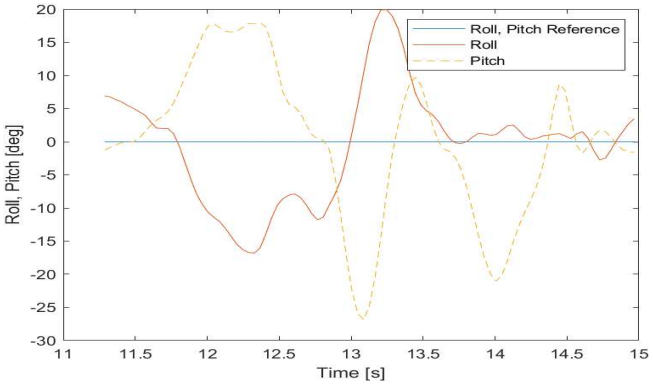

Fig. 16. Transition Roll and Pitch Attitude Plot

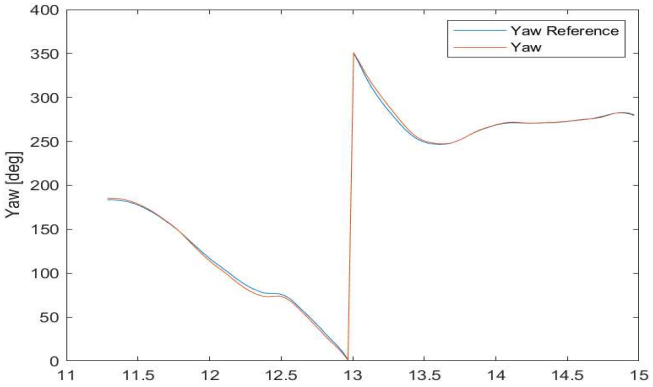

Fig. 17. Transition Yaw Attitude Plot

D. PX4 Results

The PX4 flight stack is hardware-compatible with most ArduPilot hardware, but differs from the ArduPilot ecosystem in how VTOL mixing is implemented, among other features. The MiniHawk-VTOL is most similar to the E-flite Convergence™, which is available as a preset in PX4. The setup process is detailed in [25], with '13012_convergence' selected for the SYS_AUTOSTART parameter.

VI. CONCLUSIONS

This paper addressed the design and build process of the MiniHawk-VTOL, a rapidly prototyped Tricopter/Fixed-Wing hybrid aircraft. Relevant validation and analysis studies were presented. Additionally, various collateral results including real-world flight testing and simulation models are covered. The developed aircraft has fully compatibility with major flight stacks such as ArduPilot and PX4, and provides sufficient volume and payload margin for hosting single-board computers and similar payloads onboard. The sum of the developed knowledge, tools, and models have been open-sourced for the robotics community to access. In the future we plan to investigate the directions of autonomous path-planning and perception in realistic mission profiles [28–32] by leveraging our relevant contributions.

REFERENCES

[1] D. Floreano and R. J. Wood, "Science, technology and the future of small autonomous drones," *Nature*, vol. 521, no. 7553, pp. 460–466, 2015.

[2] C. Papachristos, K. Alexis, and A. Tzes, "Design and experimental attitude control of an unmanned tilt-rotor aerial vehicle," in *2011 15th International Conference on Advanced Robotics (ICAR)*. IEEE, 2011, pp. 465–470.

[3] C. Papachristos, K. Alexis, and A. Tzes, "Towards a high-end unmanned tri-tiltrotor: Design, modeling and hover control," in *2012 20th Mediterranean Conference on Control & Automation (MED)*. IEEE, 2012, pp. 1579–1584.

[4] C. Papachristos, K. Alexis, and A. Tzes, "Hybrid model predictive flight mode conversion control of unmanned quad-tiltrotors," in *2013 European Control Conference (ECC)*. IEEE, 2013, pp. 1793–1798.

[5] C. Papachristos and A. Tzes, "Modeling and control simulation of an unmanned tilt tri-rotor aerial vehicle," in *2012 IEEE International Conference on Industrial Technology*. IEEE, 2012, pp. 840–845.

[6] C. Papachristos, K. Alexis, and A. Tzes, "Efficient force exertion for aerial robotic manipulation: Exploiting the thrust-vectoring authority of a tri-tiltrotor uav," in *2014 IEEE international conference on robotics and automation (ICRA)*. IEEE, 2014, pp. 4500–4505.

[7] C. Papachristos, K. Alexis, and A. Tzes, "Technical activities execution with a tiltrotor uas employing explicit model predictive control," *IFAC Proceedings Volumes*, vol. 47, no. 3, pp. 11 036–11 042, 2014.

[8] C. Papachristos, K. Alexis, and A. Tzes, "Dual–authority thrust–vectoring of a tri–tiltrotor employing model predictive control," *Journal of intelligent & robotic systems*, vol. 81, no. 3-4, pp. 471–504, 2016.

[9] A. Noth, "Design of solar powered airplanes for continous flight," Ph.D. dissertation, ETH Zurich, 2008.

[10] R.-A. Peloquin, D. Thibault, and A. L. Desbiens, "Design of a passive vertical takeoff and landing aquatic uav," *IEEE Robotics and Automation Letters*, vol. 2, no. 2, pp. 381–388, 2016.

[11] É. Tétreault, D. Rancourt, and A. L. Desbiens, "Active vertical takeoff of an aquatic uav," *IEEE Robotics and Automation Letters*, vol. 5, no. 3, pp. 4844–4851, 2020.

[12] J. T. VanderMey, "A tilt rotor uav for long endurance operations in remote environments," Ph.D. dissertation, Massachusetts Institute of Technology, 2011.

[13] Y. O. Aktas, U. Ozdemir, Y. Dereli, A. F. Tarhan, A. Cetin, A. Vuruskan, B. Yuksek, H. Cengiz, S. Basdemir, M. Ucar *et al.*, "A low cost prototyping approach for design analysis and flight testing of the turac vtol uav," in *2014 International Conference on Unmanned Aircraft Systems (ICUAS)*. IEEE, 2014, pp. 1029–1039.

[14] S. Carlson, "MiniHawk-VTOL," feb 2021, original-date: 2020-06-15T22:15:39Z. [Online]. Available: https://github.com/StephenCarlson/MiniHawk-VTOL

[15] S. Carlson, "A hybrid tricopter/flying-wing vtol uav," in *52nd Aerospace Sciences Meeting*, 2014, p. 0016.

[16] Z. Haider, M. S. Atif, S. Mansoor, and M. N. Bhatti, "Modeling, design and implementation of hybrid fixed-wing tri-copter," in *2019 22nd International Multitopic Conference (INMIC)*. IEEE, 2019, pp. 1–6.

[17] J. A. Bautista, A. Osorio, and R. Lozano, "Modeling and analysis of a tricopter/flying-wing convertible uav with tilt-rotors," in *2017 International Conference on Unmanned Aircraft Systems (ICUAS)*. IEEE, 2017, pp. 672–681.

[18] C. Chen, J. Zhang, D. Zhang, and L. Shen, "Control and flight test of a tilt-rotor unmanned aerial vehicle," *International Journal of Advanced Robotic Systems*, vol. 14, no. 1, p. 1729881416678141, 2017.

[19] SunPower, "SunPower Maxeon Gen III Solar Cells," oct 2020. [Online]. Available: https://us.sunpower.com/solar-resources/sunpower-maxeon-gen-iii-solar-cells

[20] S. Paudel, S. Rana, S. Ghimire, K. K. Subedi, and S. Bhattrai, "Aerodynamic and stability analysis of blended wing body aircraft," *International Journal of Mechanical Engineering and Applications*, vol. 4, no. 4, pp. 143–151, 2016.

[21] A. Deperrois, "Xflr5 stability and analysis," 2010. [Online]. Available: http://www.xflr5.tech/docs/XFLR5_and_Stability_analysis.pdf

[23] K. Alexis, C. Papachristos, R. Siegwart, and A. Tzes, "Robust model predictive flight control of unmanned rotorcrafts," *Journal of Intelligent & Robotic Systems*, vol. 81, no. 3-4, pp. 443–469, 2016.

[24] C. Papachristos, K. Alexis, and A. Tzes, "Model predictive hovering-translation control of an unmanned tri-tiltrotor," in *2013 IEEE International Conference on Robotics and Automation*. IEEE, 2013, pp. 5425–5432.

[25] "E-flite Convergence Tiltrotor VTOL (Pixfalcon) | PX4 User Guide." [Online]. Available: https://docs.px4.io/master/en/frames_vtol/vtol_tiltrotor_eflite_convergence_pixfalcon.html

[26] "Tilt Rotor Planes — Plane documentation." [Online]. Available: https://ardupilot.org/plane/docs/guide-tilt-rotor.html

[27] J. G. Ziegler, N. B. Nichols *et al.*, "Optimum settings for automatic controllers," *trans. ASME*, vol. 64, no. 11, 1942.

[28] C. Papachristos, M. Kamel, M. Popović, S. Khattak, A. Bircher, H. Oleynikova, T. Dang, F. Mascarich, K. Alexis, and R. Siegwart, "Autonomous exploration and inspection path planning for aerial robots using the robot operating system," in *Robot Operating System (ROS)*. Springer, Cham, 2019, pp. 67–111.

[29] C. Papachristos, S. Khattak, and K. Alexis, "Uncertainty-aware receding horizon exploration and mapping using aerial robots," in *2017 IEEE international conference on robotics and automation (ICRA)*. IEEE, 2017, pp. 4568–4575.

[30] C. Papachristos, K. Alexis, L. R. G. Carrillo, and A. Tzes, "Distributed infrastructure inspection path planning for aerial robotics subject to time constraints," in *2016 international conference on unmanned aircraft systems (ICUAS)*. IEEE, 2016, pp. 406–412.

[31] T. Dang, C. Papachristos, and K. Alexis, "Autonomous exploration and simultaneous object search using aerial robots," in *2018 IEEE Aerospace Conference*. IEEE, 2018, pp. 1–7.

[32] F. Mascarich, T. Wilson, C. Papachristos, and K. Alexis, "Radiation source localization in gps-denied environments using aerial robots," in *2018 IEEE International Conference on Robotics and Automation (ICRA)*. IEEE, 2018, pp. 6537–6544.